Far-Field Acoustic Imaging Enhancement Using Compact Graded Refractive Index Metamaterials

Zan Li, Jinyu Ma, Jian Li, and Xinjing Huang

***Abstract*—Acoustic metamaterials (AMMs) are promising in high-performance acoustic detection and imaging; however, few can be combined with sensors to form a practical detector, and most imaging attempts use under near-field conditions. This article provides a systematic method of using a compact graded refractive index (GRIN) AMM with an embedded microelectromechanical systems (MEMS) microphone to enhance far-field acoustic sensing and imaging. The GRIN AMM device has frequency selective amplification capability and noticeable directivity; these attributes can increase the detection range, suppress the aliasing of the multitarget main and grating lobes, and support arrays with large element separation and high angular resolution. An imaging enhancement mechanism using the GRIN AMMs is proposed and elucidated. Experiments demonstrate that the improved phased array with compact AMMs can image a 315 mm pipe as far as 67 m away and has an angular resolution up to 0.76°. Finally, the improved acoustic imaging system with an AMM array is transplanted to an FPGA-based robot to demonstrate active acoustic target-tracking application in the field.**

***Index Terms*—Acoustic imaging, acoustic metamaterials, acoustic sensing, graded refractive indices.**

I. Introduction

ACOUSTIC metamaterials (AMMs) are artificially periodic composite structures that have attracted much attention for their ability to manipulate acoustic waves and have developed rapidly over the past two decades. AMMs have unique properties that cannot be found in natural materials, such as negative equivalent density, negative equivalent bulk modulus, negative equivalent refractive index, gradient refractive index and very large refractive index. Due to these characteristics, AMMs can perform the functions of amplification, deflection, absorption, filtering, and deceleration on acoustic waves and can be applied in many areas, including acoustic cloaking, sound absorption, noise reduction, weak signal detection, and acoustic localization [1], [2], [3], [4].

In addition to the applications mentioned above, AMMs can also be further used for acoustic focusing and imaging. Conventional acoustic focusing and imaging are usually achieved by using acoustic lenses or phased arrays, and the introduction of the AMMs into conventional methods is expected to improve the resolution and contrast with small device sizes, providing a variety of potential applications [5]. For example, many researchers have designed AMM devices, including acoustic superlenses, hyperlenses, metalenses, and metasurfaces, to break the diffraction limit and achieve subwavelength focusing and imaging [6], [7], [8], [9], [10], [11]. AMM can also be used in medical imaging [12], [13], [14], which can improve the penetration depth and signal-to-noise ratio of ultrasound in human tissues. In these studies on AMM imaging, the target to be detected is placed near the AMM, and AMMs are used for near-field super-resolution imaging. Moreover, many acoustic imaging application scenarios are far-field, such as leak detection [15] and sound source localization (e.g., vehicle honking [16], high voltage partial discharge [17], seafloor topography survey [18], [19]), where the distance R between the target and the microphone/sonar array satisfies $R>2D^2/\lambda$, wherein D is the array aperture and λ is the wavelength. In the far field, a serious attenuation of the acoustic signal is present; thus, it is necessary to study how to use AMMs to improve the signal-to-noise ratio of the received signal with useful information.

There are two methods for applying AMMs to far-field imaging. One is to use metamaterial lenses to transfer subwavelength information contained in the near field to the far field. Song proposed an acoustic magnifying lens for far-field high-resolution imaging based on transformation acoustics and effective medium theory and achieved far-field high-resolution imaging with impedance matched to that of free space [20]. Orazbayev used locally resonant AMM lenses to convert evanescent waves containing subwavelength information into radiation waves and transmitted them to the far field, where neural networks were used to directly identify and image most subwavelength features [21]. In addition to the method of transferring near-field waves to far-field waves, another concept is to enhance the weak acoustic signal and improve the sensitivity of the detection device using AMMs. Moreover, many AMMs used for focusing have signal amplification effects, which can be used to enhance weak acoustic signals. Li designed an acoustic magnifying lens based on a compact nondispersive spiral metamaterial array; the incident wave could be focused on the preset point,

Manuscript received 20 March 2023; revised 7 September 2023 and 22 September 2023; accepted 30 September 2023. Date of publication 4 October 2023; date of current version 13 October 2023. This work was supported in part by the National Natural Science Foundation of China under Grant 62073233, in part by the Natural Science Foundation of Tianjin City under Grant 21JCQNJC00690, and in part by the State Key Laboratory of Precision Measurement Technology and Instruments under Grant pilab2104. The associate editor coordinating the review of this manuscript and approving it for publication was Prof. A. F. Frangi. *(Corresponding author: Xinjing Huang.)*

The authors are with the State Key Laboratory of Precision Measurement Technology and Instruments, School of Precision Instrument and Optoelectronics Engineering, Tianjin University, Tianjin 300072, China (e-mail: lizan@tju.edu.cn; jinyu.ma@tju.edu.cn; tjupipe@tju.edu.cn; huangxinjing@tju.edu.cn).

This article has supplementary downloadable material available at https://doi.org/10.1109/TCI.2023.3321994, provided by the authors.

Digital Object Identifier 10.1109/TCI.2023.3321994

and the pressure amplitude could be increased by approximately three times [22]. Kim proposed a metamaterial lens that could focus acoustic waves; the signals passing through the lens were enhanced two times, and underwater ultrasonic imaging was achieved [23]. Chu proposed a space-coiling gradient AMM for acoustic enhancement and weak signal detection, and the sound pressure amplitude was amplified by more than 30 times [24]. These AMM devices were large in size, and their amplification factors were not that significant; thus, the efficiency of acoustic detection enhancement was low. To achieve far-field imaging with higher performance, to the combination of the enhancement effect of AMMs with phased arrays or other technologies is feasible. In addition to a high amplification factor and small size, the AMM needs to also be adapted to conventional acoustic sensors, such as microphones to form a practical detector.

Among the various types of AMMs, a new class of dispersive AMMs with graded refractive index (GRIN) shows great promise for these applications. Acoustic waves can be decelerated and trapped by the GRIN AMM, which provides a promising prospect in acoustic sensing enhancement and precise spatial-spectral control of acoustic waves. For the first time, Zhu experimentally demonstrated a GRIN AMM consisting of an array of grooves perforated on a rigid bar that trapped broadband acoustic waves and spatially separated different frequency components; this was called the acoustic rainbow trapping (ART) effect [25]. Chen proposed an anisotropic GRIN AMM waveguide composed of a periodic array of rectangular steel plates with linearly changed widths spaced by air gaps with equal thickness; this metamaterial achieved a noticeable ART effect as well as enhanced acoustic sensing through acoustic wave compression and pressure amplification [26]. Afterward, researchers designed a variety of GRIN AMMs that have ART effects, which were composed of plate arrays [27], [28], [29], [30], groove arrays [24], [31], [32], [33] or resonant cavity arrays [34], and the array arrangements were linear or spiral. These AMMs had the functions of multiband acoustic enhancement, weak signal detection and localization, frequency selection, etc.; however, their size in one direction was too large to form an array, which was not convenient. This problem could be solved by using an axisymmetric AMM. For example, the conical GRIN AMM designed by Huang [35] had excellent acoustic pressure amplification and multiband filtering capability; a microelectromechanical systems (MEMS) microphone was embedded into the AMM to constitute a sensor, and it did not weaken its acoustic wave manipulation performance. Therefore, this AMM device could be used to build acoustic arrays. Yazdkhasti used downsized AMMs proposed by Huang to form an array for acoustic imaging, and the farthest imaging distance of the pipes reached 15 meters under laboratory conditions [36]. These AMMs have promising characteristics, but most of their research remains in the stage of numerical simulation and laboratory testing. A significant contribution is to achieve the practical application of AMMs in acoustic sensing. In this article, the GRIN AMM is used to enhance far-field acoustic imaging due to its amplification capability and available compact size for forming an array. The enhancement mechanism of the GRIN AMM on the acoustic imaging performance needs to be further clarified, and the advantages of the GRIN AMM need to be further explored.

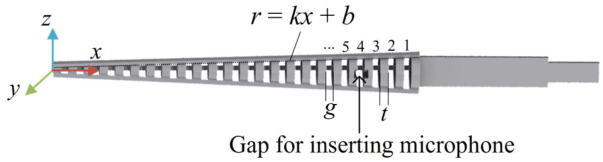

Fig. 1. 3D model of the proposed GRIN AMM.

This article proposes a method using a compact conical GRIN AMM with an embedded MEMS microphone to enhance the far-field acoustic sensing and imaging. Both simulations and experiments are performed to examine the acoustic amplification capacity and specific directivity of the AMM device. The principle of far-field phased array imaging enhancement by using GRIN AMMs is analyzed, proposed and elucidated based on the device characteristics. Several experiments are performed with the imaging testing system to compare the imaging performances with and without AMMs. Finally, the improved phased array equipped with the AMMs is applied in long-distance echolocation and target tracking executed by an FPGA-based acoustic imaging robot.

II. Principle and Method

A. GRIN AMM Design and Test

The proposed GRIN AMM, as shown in Fig. 1, consists of a series of circular plates with gradient radii that are described by the following equation: $r = kx + b$ (the outline satisfies the same equation). In the model, r is the radius of each circular plate, k is the gradient of the radius along the x-axis, b is the radius of the smallest plate when $x = 0$, t is the thickness of each plate, and g is the width of the gap between the plates. The gaps are numbered with 1, 2, 3, …, from right to left.

According to [26], the effective refractive index of the GRIN AMM is always greater than that of air, gradually increases along the x-axis direction, and sharply increases at a certain position. Therefore, the AMM can shorten the wavelength of the acoustic wave propagating along the axis, reduce the sound speed, finally concentrate the energy in a small area in the AMM, and cause strong pressure enhancement. This effect is achieved by the dispersive modulation of the sound speed through gradually varying subwavelength unit cells that are strongly coupled along the propagation direction. The acoustic wave propagating along the surface of the AMM lengthens its equivalent sound path due to the interaction with the acoustic pressure in the gaps, and therefore, the equivalent acoustic refractive index gradually becomes increasingly larger due to sound path accumulation along the acoustic wave propagation direction. Moreover, the AMM waveguide can also help overcome the wave vector and mode-field mismatch between the AMM and air, thus enabling a high coupling efficiency. In summary, the AMM can capture a certain width of the plane acoustic waves near the waveguide, longitudinally compress and amplify the internal acoustic waves, and finally focus the specific frequency of the acoustic waves at a certain position in the AMM.

Low-frequency acoustic waves are concentrated in the gap with a larger diameter, while high-frequency acoustic waves are concentrated in the gap with a smaller diameter. By adjusting the parameters of the equation $r = kx + b$ and inserting a microphone in the appropriate gap, the capture and amplification of any frequency acoustic wave can be achieved. If the size of the AMM is reduced, all working frequencies are increased. Notably, the ratio of the thickness to the width of the gap or plate needs to be matched. Decreasing the gap thickness results in an increase in the pressure gain; however, further narrowing the gap thickness leads to a decrease in the pressure gain, which is believed to be the result of more significant dissipation due to the air viscous effect and thermal loss in smaller air channels [26]. Moreover, if the plate is too thin, the rigidity will be lowered, the plate will easily couple and resonate together with the air cavity, and the sound energy in the air will thus be lost. Finally, a set of geometric parameters of the device is determined as follows: the radii $r = 0.04139x + 1.06$ mm, the thickness t of each plate is 2 mm, the gap g is 1.6 mm, and the total length excluding the handle is 84.8 mm. The working frequency of several gaps at the large end of this device is 20 kHz-30 kHz. To adjust the working frequency, the geometric parameters of the AMM device only need to be proportionally adjusted.

A 2D axisymmetric finite element simulation of the proposed GRIN AMM is conducted with COMSOL software. Fig. 2(a) shows the simulation model. The material of the entire model is air, and the model is split into two domains: the pressure acoustics domain and the thermoviscous acoustics domain. The former is set to 0.2 m × 0.05 m, and the latter is set to 0.09 m × 0.008 m and exactly surrounds the AMM. Perfectly matched layers are applied to the right and bottom boundaries. The plane wave is incident from the left boundary, the acoustic pressure is 1 Pa, and the frequency sweeping range is 1 kHz to 40 kHz. Fig. 2(b) shows the absolute acoustic pressure field inside and outside the AMM at multiple frequencies. The bright spots indicate where the acoustic waves concentrate and are amplified. Fig. 2(c) shows the spatial distribution of the absolute acoustic pressure along the symmetry axis at multiple frequencies. According to the simulation results, the AMM has noticeable amplification of the incident acoustic wave, and the waves of different frequencies are concentrated in specific different gaps. For 25 kHz waves, the acoustic pressure reaches the maximum value in Gap 4. Fig. 2(d) shows the relationship between the acoustic pressure in several gaps and the incident wave frequency. For Gap 4, only 25 kHz waves are greatly amplified.

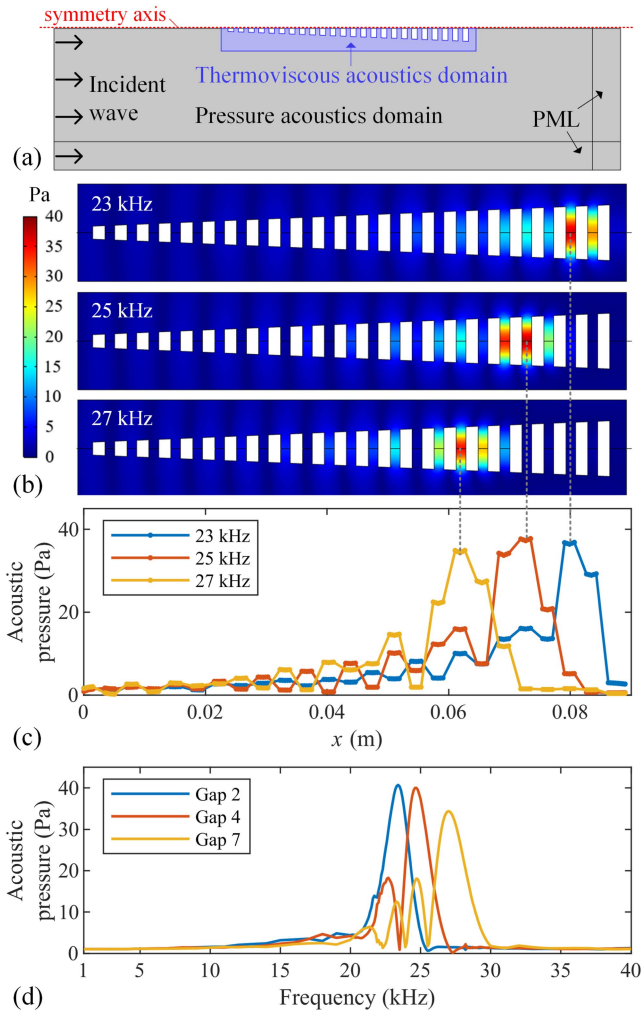

Fig. 2. Finite element simulation of the AMM. (a) Configuration of the 2D axisymmetric simulation model. (b) Absolute acoustic pressure fields inside and outside the AMM at 23, 25, and 27 kHz. (c) Spatial distributions of the absolute acoustic pressure along the x-axis at 23, 25, and 27 kHz. (d) Acoustic pressure at the 2nd, 4th, and 7th gaps from 1 kHz-40 kHz.

The gain spectrum and directivity of the AMM device are tested using the experimental apparatus shown in Fig. 3(a). The apparatus consists of a broadband loudspeaker, a rotary table, a power supply and signal acquisition board, and an AMM device. The AMM device shown in Fig. 3(b) is 3D-printed with stereolithography (SLA) process, and the material is photosensitive resin (UTR9000). A tiny slot is embedded at the gap near the large end for attaching the MEMS microphone. The MEMS microphone (model number: SPU0410LR5H-QB) is tiny-sized (3.76 mm × 3 mm × 1.1 mm) and omnidirectional. Experiments are carried out in an open field where the acoustic plane waves emitted by a broadband loudspeaker are coupled from free space into the AMM device. The AMM device is bonded on a rod attached to a rotary table. The signals emitted by the speaker are a series of sinusoidal waves modulated by a Hanning window with a sweeping frequency range of 1 kHz to 40 kHz. Output signals of the microphone with and without AMM are separately acquired.

The output amplitudes of the microphone with and without the AMM from 1 kHz-40 kHz and the acoustic gain spectrum of the AMM are shown in Fig. 3(c). The acoustic gain of the AMM is calculated by normalizing the outputs with the AMM to the outputs without the AMM. The microphone with the AMM has a prominent frequency response at 25 kHz and a large acoustic gain of 17.3 times, while at other frequencies, the amplification is not as large; this result confirms that the AMM has the capacity of frequency selective amplification detection. As shown in Fig. 3(d), the omnidirectional microphone demonstrates noticeable directivity after being inserted into the AMM. The directivity of the AMM can be used to suppress

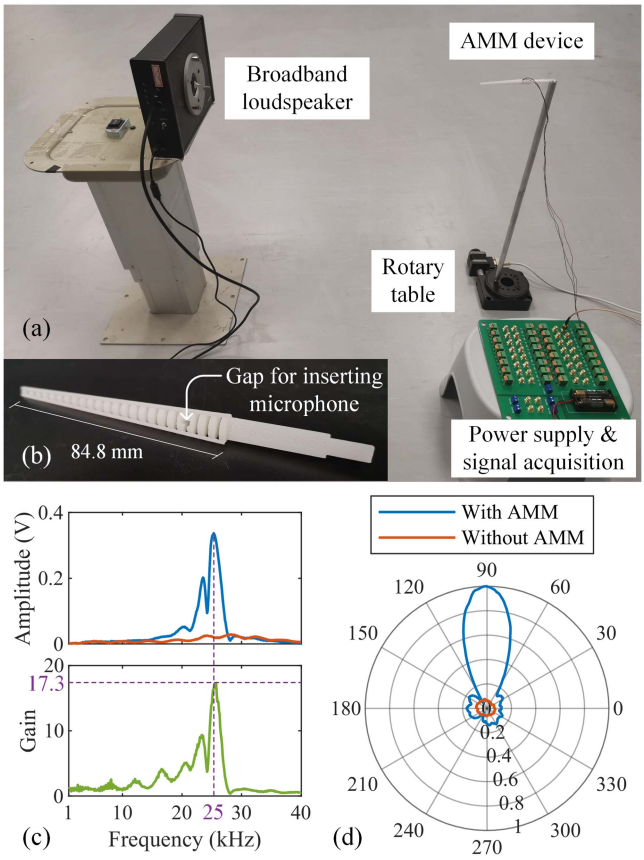

Fig. 3. Tests of the acoustic amplification capacity and directivity of a single AMM. (a) Experimental apparatus. (b) 3D-printed AMM device. (c) Frequency responses of the microphone with and without the AMM and the acoustic gain spectrum of the AMM. (d) Directivity patterns with and without the AMM.

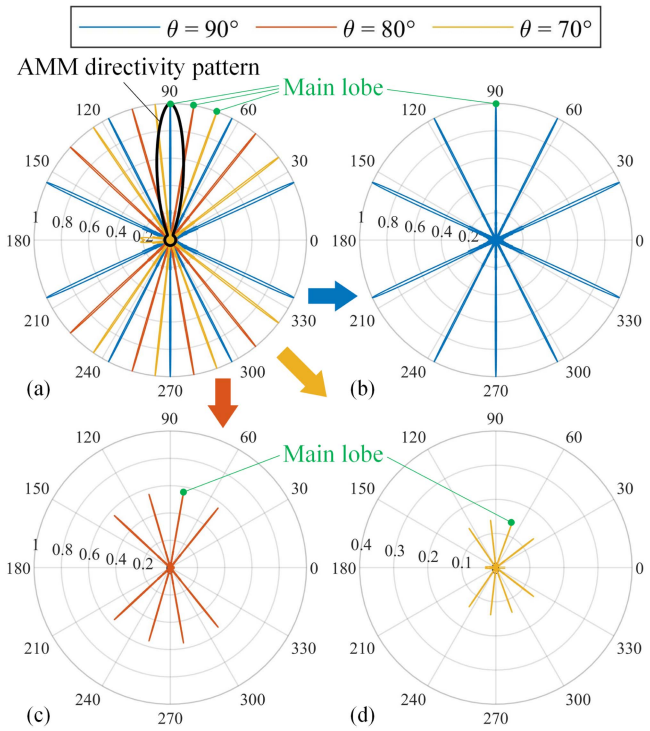

Fig. 4. Array directivity patterns (a) without and (b–d) with AMMs when multiple sound sources are incident from 90°, 80° and 70°, respectively; the array configuration is $\lambda = 0.45d$, $N = 32$.

the grating lobe interference and is, thus, helpful for building a large-aperture high-resolution acoustic imaging array.

B. Phased Array Imaging Enhancement by AMMs

The far-zone field of a uniform N-element array of identical elements is equal to the product of the field of a single element at a selected reference point (usually the origin) and the array factor of that array [37], as follows:

$$E(\text{total}) = [E(\text{single element at reference point})] \times [\text{AF}(\text{array factor})]. \quad (1)$$

The array factor of the N-element linear array is as follows:

$$\text{AF} = \left[\frac{\sin\left(\frac{N}{2}\psi\right)}{\sin\left(\frac{1}{2}\psi\right)}\right], \quad (2)$$

where $\psi = kd\cos\theta + \beta$, $k = 2\pi/\lambda$ is the wave vector, λ is the wavelength, d is the element separation, θ is the angle between incident waves and the array, and β is the artificially attached phase increment on receiving signals. Therefore, increasing the signal of a single element can increase the signal-to-noise ratio of the whole array and can help detect farther. The 3-dB point for the array factor of (2) occurs when the following condition is met:

$$\theta_h = \cos^{-1}\left[\frac{\lambda}{2\pi d}\left(-\beta \pm \frac{2.782}{N}\right)\right]. \quad (3)$$

where θ_h is also the angular resolution of the array. When λ is fixed, θ_h decreases (which means higher resolution) with increasing array element separation d and number of array elements N. However, when $d > \lambda/2$, grating lobes (i.e., virtual image) appear. A larger d correlates to more grating lobes. When there is only one target in the field of view of the array, the main lobe, which is the true azimuth of the target, is easily determined, as shown by each colored curve in Fig. 4(a), because the main and grating lobes with fixed patterns have their own explicitly known azimuths. However, when there are multiple targets in the field of view, the main and grating lobes of different targets will be aliased together, as shown by different colored curves in Fig. 4(a), and it is impossible to determine the corresponding main lobes of each target from those aliased lobes.

According to (1), the actual array directivity is the directivity of a single element (i.e., the directivity of the AMM) multiplied by the array factor. After attaching the AMMs to each array element (microphone), the main and grating lobes outside the field of view determined by the AMM directivity is suppressed, as shown in Fig. 4(b)–(d). The AMM directivity pattern narrows the array's field of view, and interferences from other directions are prevented. This array focuses on the preocular field of view while allowing the existence of grating lobes with large element separation and very high angular resolution, and the view can be expanded by rotating the array. Therefore, the AMMs can

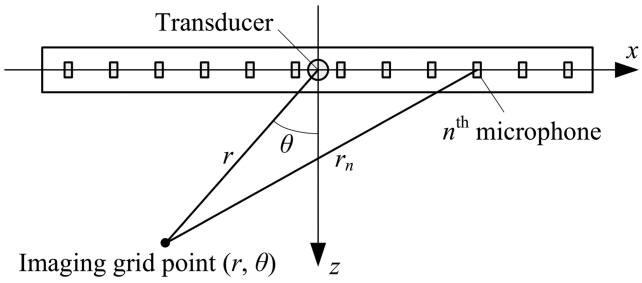

Fig. 5. Diagram of the adopted beamforming algorithm.

enhance phased array imaging by using its directivity to suppress the grating lobe interferences to achieve high angular resolution and using its amplification effect to improve the signal-to-noise ratio to increase the detection range.

C. Phased Array Imaging Algorithm

The conventional time-domain beamforming algorithm is adopted to calculate the echo amplitude of each grid point in the view to be imaged, as shown in Fig. 5. The procedures are as follows [38]:

1) The imaging area is divided into many grid points. The grid point positions are marked as (r, θ) in polar coordinates.
2) The distance r between the transducer and each grid point and the distance r_n between each grid point and the n^{th} microphone are calculated.
3) The echo signals output by the microphones are delayed and added up to obtain the beamforming signal. The synthesized beamforming signal $Y(t)$ at grid point (r, θ) is as follows:

$$Y(t) = \sum_{n=1}^{N} y_n \left(t + \frac{r + r_n}{c} \right), \tag{4}$$

where $y_n(t)$ is the output signal of the n^{th} microphone and c is the sound speed.
4) The spectral amplitude A of the synthesized beamforming signal is calculated, and the acoustic image $A(r, \theta)$ can be obtained.

III. Imaging Enhancement Tests

The imaging testing system, as shown in Fig. 6, consists of DAQ boards (NI PXIe 6378) and an imaging computer (NI PXIe 8881), an ultrasonic transmitter (TCT25-16T), and a microphone array with 32 elements and a uniform element separation of 30 mm. The microphones can be supported by the AMMs or a specially designed holder for experiments without the AMM. The speaker is fixed above the center point of the array and driven by the signals generated by the DAQ boards and sequentially amplified by a power amplifier. The emitting sound is 25 kHz. The signal is reflected by the target, and the echo signal is sensed by the array and acquired by the DAQ boards. The computer processes the array data and displays the image on the screen. The subgraph in Fig. 6 is the result of the acoustic imaging of two pipes at approximately 37 m.

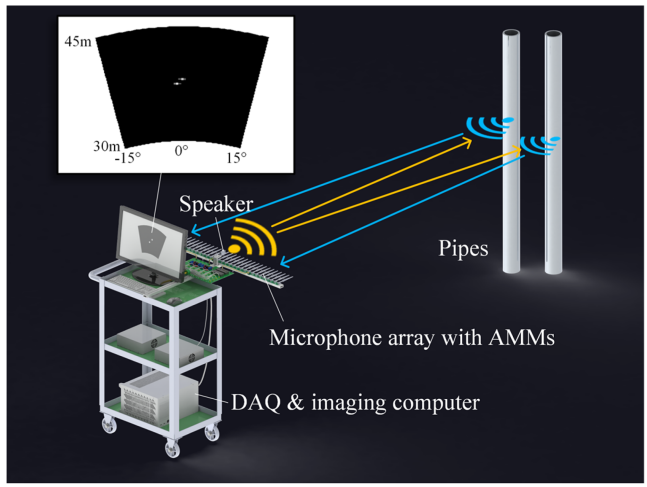

Fig. 6. Imaging testing system for the microphone array with the AMMs.

A. Detection Capacity Testing

To demonstrate the detection capability, two sets of tests were carried out: imaging of pipes with different diameters and imaging of the same pipe at different distances.

In the first group of imaging experiments, aluminum and PVC pipes with diameters of 10 mm, 20 mm, 30 mm, 40 mm, 60 mm, 100 mm, and 200 mm were placed at approximately 35 m from the imaging testing system, and these pipes were separately imaged with and without the AMMs. The amplitude data of the images are plotted in Fig. 7(a). Multiple points of the same diameter represent the results of multiple repeated snapshots. All 10–200 mm pipes were successfully imaged by the array with AMMs. The amplitudes with the AMMs were significantly higher than those without AMMs, and the 10 mm and 20 mm pipes could not be imaged when the AMMs were not used.

In the second group of imaging experiments, a 315 mm PVC pipe was placed at distances of 9 m, 19 m, 29 m, 39 m, 49 m, 59 m, and 67 m away from the imaging testing system, and the pipe was separately imaged with and without the AMMs. The amplitude data of the images are plotted in Fig. 7(b). Multiple points at the same distance represented the results of multiple repeated snapshots. Because of the large differences in the amplitudes, the vertical coordinate was on a logarithmic scale. The amplitudes with the AMMs were significantly higher than those without the AMMs, and the amplitude decreased as the distance increased. The maximum imaging distance was 67 m with the AMMs and only 49 m without the AMMs. Moreover, the holder itself could amplify the acoustic pressure two times; thus, it is speculated that the maximum imaging distance without the AMMs was only $49/\sqrt{2} = 35$ m, which was only half of that with the AMMs; this result demonstrated the advantage of AMM in detecting the target at a long distance.

Two sets of data with and without AMMs at 49 m were used to calculate the spectra of all 32 signals, and the results are illustrated in Fig. 7(c). The spectra with the AMMs had very prominent peaks near 25 kHz, while the spectra without the AMMs had other peaks besides the inapparent 25 kHz peak. The peak value with AMMs was approximately 8 times as high as

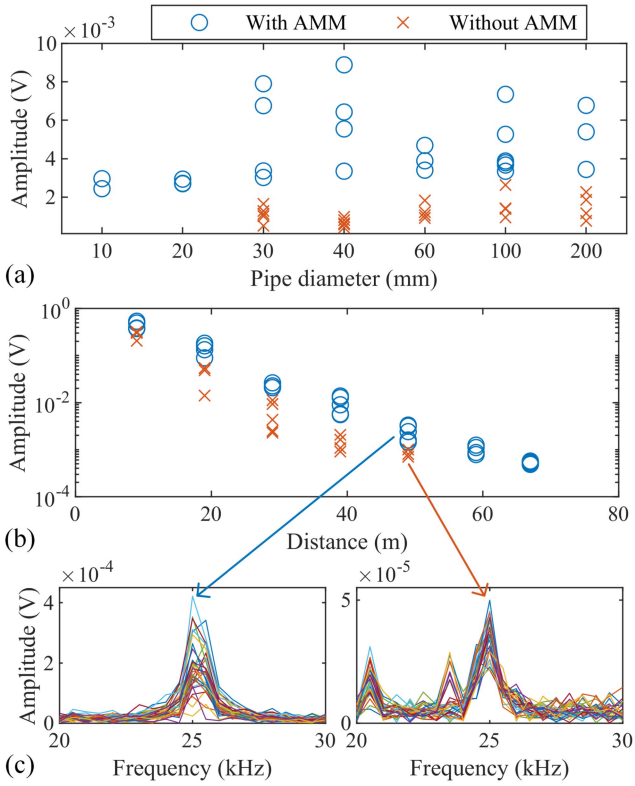

Fig. 7. Comparison experiments of the imaging performances with and without the AMMs (a) with different pipe diameters at the same distance and (b) at different distances with the same pipe. (c) Comparison of the echo spectra of the 32 microphones with and without the AMMs at 49 m.

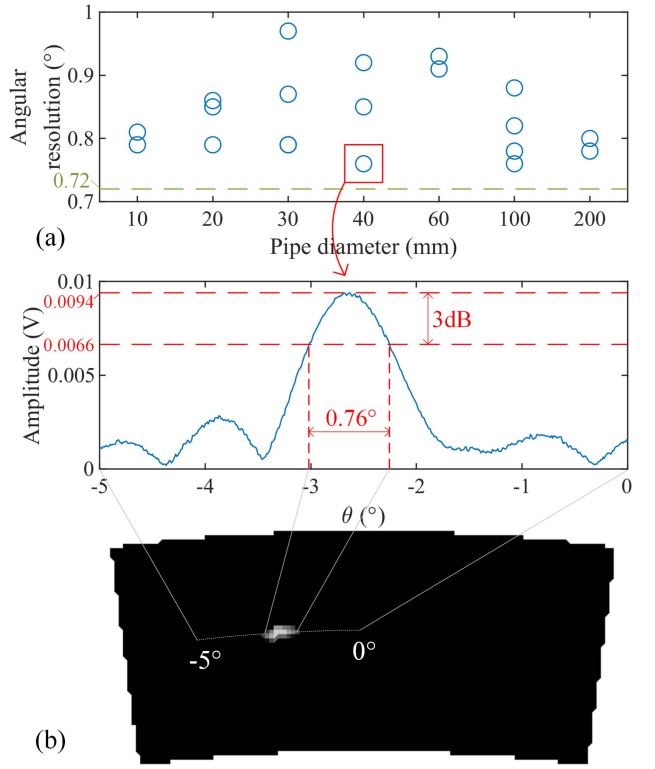

Fig. 8. Angular resolution of the microphone array with the AMMs. (a) Angular resolutions calculated with different pipe diameters. (b) Calculating the angular resolution for a specific experiment as a demonstration.

that without AMMs, which confirmed the outstanding frequency selective amplification effect of the AMM.

B. Angular Resolution Verification

In air, for an array of $N = 32$, $d = 30$ mm and acoustic waves of 25 kHz and considering $\beta = 0$ when the target is directly in front of the array, the theoretical imaging angular resolution can be calculated using (3) as follows:

$$\begin{aligned}\theta_h &= \cos^{-1}\left[\frac{\lambda}{2\pi d}\left(\pm\frac{2.782}{N}\right)\right] \\ &= \cos^{-1}\left[\frac{13.6\text{mm}}{2\pi \times 30\text{mm}}\left(\pm\frac{2.782}{32}\right)\right] \\ &= 0.72^\circ \end{aligned} \tag{5}$$

The angular resolution is the angular width when the amplitude decreases from the peak point to 3 dB at the same distance. Based on this definition, the angular resolutions for the imaging experiments of different pipes at 30 m are calculated and illustrated in Fig. 8(a). The imaging angular resolution of the microphone array with AMMs is within 1° and up to 0.76°, which is close to the theoretical value. The angular resolution for a specific experiment is calculated as a demonstration, which is shown in Fig. 8(b).

C. Grating Lobe Interference Suppression

A larger array element separation correlates to a higher imaging angular resolution; however, when the array element separation is too large, a virtual image caused by the grating lobes appears. According to Section II, the directivity of the AMM is one of the keys to ensuring the success of a phased array with a large element separation, high resolution and the presence of grating lobes. The sector region surrounded by the AMM directivity curve in Fig. 4(a) is the visible range of the AMM. Within the visible range, the target can be imaged normally; when the target exceeds the visible range, the imaging becomes suppressed and extremely weak, as shown in Fig. 4(b)–(d). In contrast, the array without the AMMs cannot suppress these lobe interferences from the side.

This effect of the AMM on the array is shown by rotating the imaging testing system and observing the change in imaging amplitude. A schematic diagram of the experiment is shown in Fig. 9(a). First, the imaging testing system is placed facing the target, and an acoustic image is captured. Then, the target is fixed, the system is rotated by θ_0 (10°, 20° and 30°) in situ, and three acoustic images are captured. The experimental results are shown in Fig. 9(b). Comparing the amplitude of the peaks, the peak value is distinctly suppressed after rotating the system; it is suppressed to 1/4 when the system rotates only 10° and is almost zero when the system rotates 30°. This experiment shows that AMM has a very noticeable suppression effect on targets beyond the field of view and can effectively prevent interference from

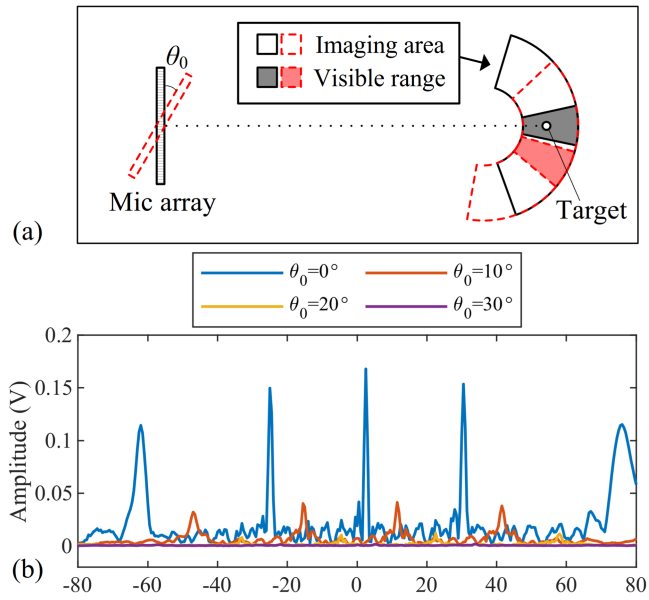

Fig. 9. Demonstration experiment of the AMM's capacity for grating lobe interference suppression. (a) Experiment diagram. (b) Imaging amplitudes with the AMMs when the array is rotated by different angles.

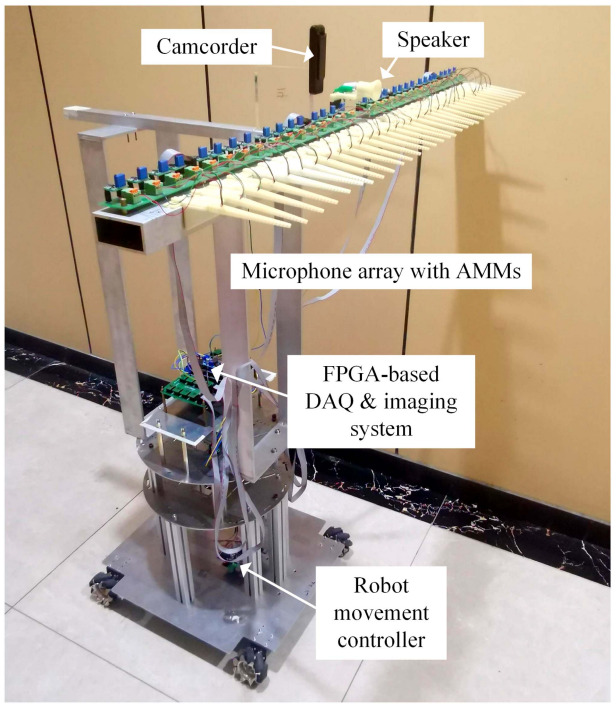

Fig. 10. Echolocation tracking system based on FPGA and microphone array with the AMMs.

signals from other directions; this result shows the beneficial effect of the AMM on imaging. The directivity of the proposed AMM can suppress the aliasing of multitarget main and grating lobes to support arrays with large element separation and high angular resolution.

IV. Echolocation Tracking Application

A. System Components

The microphone array with AMMs is transplanted into a target tracking system based on echolocation, as shown in Fig. 10. Compared with the previous imaging system, the entire DAQ and imaging algorithm are executed by an FPGA controller. A robot platform is equipped into the system as a subsystem to control the movement of all the parts, and a camcorder is used to record the scene straight ahead. The FPGA is responsible for (a) control of generating transmission signals and acquiring microphone array signals, (b) execution of target imaging as well as target azimuth and distance extraction, and (c) sending instructions to the robot movement controller according to the preset tracking strategy. The robot drives the entire tracking system to move forward or rotate and adjust its azimuth angle according to the received instructions. The tracking experiment is carried out in an open field, which is also the test ground of Section III, as shown in Fig. 11(a). The experimenter walks in the field as a moving target, and the robot continuously images and tracks the target. The experiment video can be found in the Supplemental Material.

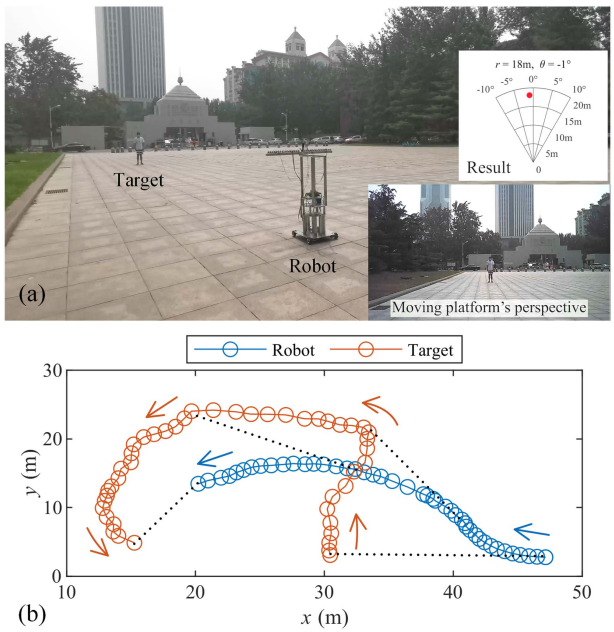

Fig. 11. Echolocation tracking application. (a) Screenshot of the demonstration video. (b) Tracks of the target and the robot.

B. Tracking Performance

The tracks of the robot and the target are plotted in Fig. 11(b). The robot is tracking and chasing the target; thus, the two tracks are not identical. At first, there is nearly 20 m between the robot and the target. When the target moves, the robot will initially rotate to face the target and then move forward for a distance. The robot can continuously track the position of the target by repeating the operations above. From the results, when the moving trend of the target greatly changes, the robot can respond and adjust in time to successfully follow the target. If the AMMs are not used, the imaging signal-to-noise ratio and

resolution of the array at the same long distance is very low, and the stability of target recognition is very poor, causing difficulty to complete the target tracking.

V. Discussion

A. AMM's Contribution to Acoustic Detection

The acoustic detection performance depends on four cascaded signal processing steps: (a) acoustic capturing, (b) acoustic-electric transition (accomplished by the sensor), (c) real-time signal conditioning (accomplished by the circuit), and (d) signal processing (accomplished by the algorithm). Our study focuses on the forefront of acoustic detection and improves the performance of acoustic capturing. The performances in steps (b)–(d) can be enhanced with the improvement of step (a). Our proposed AMM can be combined with other existing acoustic sensors and signal processing techniques in series, and the performance using any single method will be further significantly improved. For example, advanced phased array beamforming algorithms (e.g., DAMAS [39] and time reversal [40]) can be used in conjunction with this AMM and obtain better performance.

B. AMM's Narrow Bandwidth

The AMM proposed in our study is narrowband, and a narrow bandwidth is not ideal for acoustic sensing and imaging; however, as for our proposed AMM, some approaches are available to address this. On the one hand, special signals suitable for narrowband sensors can be used for emission. For example, Laureti used a narrowband acoustic transducer with a −3 dB bandwidth of 5 kHz centered at 40 kHz to achieve acoustic detection with frequency modulation, which in turn enabled the localization of close-range unmanned ground vehicles [41]. The proposed AMM had a −3 dB bandwidth of 5 kHz centered at 25 kHz, as shown in Figs. 2 and 3; thus, the frequency band of our proposed AMM is wide enough to achieve this narrow frequency modulation.

On the other hand, the bandwidth of our proposed AMM can be further broadened. A feasible approach is to insert microphones into multiple gaps and simultaneously capture the signals of multiple frequency bands. Then, the signals can be added up with an adder circuit or addition program, and a broadband signal is obtained. This concept is based on the fact that the frequency response of the microphone in each gap has a certain bandwidth, and adding up the signals of multiple gaps produces a broadband signal.

C. Considerations of AMM's Usage in Other Scenarios

The AMM can also be moved to other application scenarios, such as ocean acoustics and medical ultrasound. However, some issues need to be considered. For example, in ocean acoustics, when the AMM is used underwater, the acoustic impedance contrast between water and solid is not as high as that between air and solid, and the vibration coupling between solid and liquid can be very serious, resulting in the loss of its frequency selective amplification capability. To maintain the same acoustic amplification and directivity of our proposed AMM in water, other materials with higher acoustic impedances can be used, such as tungsten and steel, or the thickness of each plate in the AMM needs to be increased. Both methods can weaken the vibration coupling between solid and liquid. A detailed study needs to be performed in future research.

VI. Conclusion

A compact conical GRIN AMM consisting of a series of circular plates with varying diameters to improve the phased array imaging performance is proposed. By changing the size of the outline dimensions and selecting different gaps to insert the microphone, the operating frequency of the AMM device can be flexibly adjusted. Simulations and experiments demonstrate that the AMM device has a remarkable directivity and frequency selective amplification capability. The improvement mechanism of the AMMs in phased array imaging is proposed and elucidated specifically, the AMM's directivity is used to suppress the grating lobe interferences to achieve high angular resolution with large element separation, and the AMM's amplification effect is used to improve the signal-to-noise ratio to increase the detection range.

Pipe imaging tests show that the microphone array with the AMMs can detect the 315 mm pipe as far as 67 m away and has an angular resolution up to 0.76°, while the microphone array without the AMMs can only detect the 315 mm pipe as far as 35 m away. The microphone array with the AMMs can image pipes as small as 10 mm in diameter at a 35 m distance, while the array without AMM can only image pipes larger than 30 mm at the same distance. Due to the long detection range and high angular resolution, an improved phased array equipped with AMMs is successfully applied in far-field echolocation and tracking demonstration on an FPGA-based robot.

Finally, some concerns regarding the usage of AMM are discussed. The AMM's contribution to acoustic detection is analyzed and highlighted. The utilization of the AMM's narrow bandwidth and methods to further broaden the bandwidth are provided. Furthermore, issues that need to be addressed when the proposed AMM is used in other applications are detailed.

References

[1] G. Liao, C. Luan, Z. Wang, J. Liu, X. Yao, and J. Fu, "Acoustic metamaterials: A review of theories, structures, fabrication approaches, and applications," *Adv. Mater. Technol.*, vol. 6, no. 5, May 2021, Art. no. 2000787, doi: 10.1002/admt.202000787.

[2] H. Song, X. Ding, Z. Cui, and H. Hu, "Research progress and development trends of acoustic metamaterials," *Molecules*, vol. 26, no. 13, Jul. 2021, Art. no. 4018, doi: 10.3390/molecules26134018.

[3] Z. Zhang, Y. Zhao, and N. Gao, "Recent study progress of underwater sound absorption coating," *Eng. Rep.*, vol. 5, 2023, Art. no. e12627, doi: 10.1002/eng2.12627.

[4] X. Sun, H. Jia, Z. Zhang, Y. Yang, Z. Sun, and J. Yang, "Sound localization and separation in 3D space using a single microphone with a metamaterial enclosure," *Adv. Sci.*, vol. 7, no. 3, Feb. 2020, Art. no. 1902271, doi: 10.1002/advs.201902271.

[5] F. Ma, Z. Huang, C. Liu, and J. H. Wu, "Acoustic focusing and imaging via phononic crystal and acoustic metamaterials," *J. Appl. Phys.*, vol. 131, no. 1, Jan. 2022, Art. no. 011103, doi: 10.1063/5.0074503.

[6] Y. Tian, H. Ge, M. H. Lu, and Y. F. Chen, "Research advances in acoustic metamaterials," *Acta Physica Sinica*, vol. 68, no. 19, Oct. 2019, Art. no. 194301, doi: 10.7498/aps.68.20190850.

[7] J. H. Oh, H. M. Seung, and Y. Y. Kim, "A truly hyperbolic elastic metamaterial lens," *Appl. Phys. Lett.*, vol. 104, no. 7, Feb. 2014, Art. no. 073503, doi: 10.1063/1.4865907.

[8] N. Kaina, F. Lemoult, M. Fink, and G. Lerosey, "Negative refractive index and acoustic superlens from multiple scattering in single negative metamaterials," *Nature*, vol. 525, no. 7567, pp. 77–81, Sep. 2015, doi: 10.1038/nature14678.
[9] C. B. Hu, J. K. Weng, Y. J. Ding, B. Liang, J. Yang, and J. C. Cheng, "Experimental demonstration of a three-dimensional acoustic hyperlens for super-resolution imaging," *Appl. Phys. Lett.*, vol. 118, no. 20, May 2021, Art. no. 203504, doi: 10.1063/5.0047131.
[10] S. Laureti, D. A. Hutchins, L. A. J. Davis, S. J. Leigh, and M. Ricci, "High-resolution acoustic imaging at low frequencies using 3D-printed metamaterials," *Amer. Inst. Phys. Adv.*, vol. 6, no. 12, Dec. 2016, Art. no. 121701, doi: 10.1063/1.4968606.
[11] H. Su, X. Zhou, X. Xu, and G. Hu, "Experimental study on acoustic subwavelength imaging of holey-structured metamaterials by resonant tunneling," *J. Acoust. Soc. Amer.*, vol. 135, no. 4, pp. 1686–1691, Apr. 2014, doi: 10.1121/1.4868395.
[12] S. S. Rojas, S. Tridandapani, and B. D. Lindsey, "A thin transducer with integrated acoustic metamaterial for cardiac CT imaging and gating," *IEEE Trans. Ultrason., Ferroelect., Freq. Control*, vol. 69, no. 3, pp. 1064–1076, Mar. 2022, doi: 10.1109/TUFFC.2021.3140034.
[13] S. S. Rojas, S. Tridandapani, and B. D. Lindsey, "A thin, high penetration depth phased array transducer with a metamaterial acoustic backing for cardiac imaging with X-ray computed tomography compatibility," in *Proc. IEEE Int. Ultrason. Symp.*, 2021, pp. 1–4, doi: 10.1109/IUS52206.2021.9593512.
[14] H. Xu, J. Shi, M. Huang, T. Li, and W. Niu, "Sensitivity enhancement of ultrasound imaging based on acoustic metamaterial," in *Proc. IEEE Int. Conf. Comput. Sci. Netw. Technol.*, 2011, pp. 2088–2092, doi: 10.1109/ICCSNT.2011.6182382.
[15] L. Li et al., "Three-dimensional localization of gas leakage using acoustic holography," *Mech. Syst. Signal Process.*, vol. 171, May 2022, Art. no. 108952, doi: 10.1016/j.ymssp.2022.108952.
[16] Z. Zhao, W. Chen, K. A. Semprun, and P. C. Y. Chen, "Design and evaluation of a prototype system for real-time monitoring of vehicle honking," *IEEE Trans. Veh. Technol.*, vol. 68, no. 4, pp. 3257–3267, Apr. 2019, doi: 10.1109/TVT.2019.2893777.
[17] J. Ramirez-Nino, R. Mijarez, and J. H. Rodriguez-Rodriguez, "Simple acoustic sensor array for partial discharge detection and location in electrical apparatus," *Meas. Control*, vol. 48, no. 4, pp. 122–128, May 2015, doi: 10.1177/0020294015569261.
[18] Z. H. Li, Y. C. Zhang, and G. H. Zhan, "Realtime mosaic and visualization of 3D underwater acoustic seabed topography," *J. Jilin Univ. (Eng. Technol. Ed.)*, vol. 52, no. 1, pp. 180–186, Jan. 2022, doi: 10.13229/j.cnki.jdxbgxb20200783.
[19] J. Zhai, B. Zou, J. Xu, and S. Gao, "Tests for performances of a high-resolution underwater imaging sonar," *J. Vib. Shock*, vol. 37, no. 2, pp. 223–227, 2018, doi: 10.13465/j.cnki.jvs.2018.2.033.
[20] G. Y. Song, W. X. Jiang, Q. Cheng, L. T. Wu, H. Y. Dong, and T. J. Cui, "Acoustic magnifying lens for far-field high resolution imaging based on transformation acoustics," *Adv. Mater. Technol.*, vol. 2, no. 9, Sep. 2017, Art. no. 1700089, doi: 10.1002/admt.201700089.
[21] B. Orazbayev and R. Fleury, "Subwavelength acoustic imaging in far field by combining metamaterials and deep learning," in *Proc. IEEE 15th Int. Congr. Artif. Mater. Novel Wave Phenomena (Metamaterials)*, 2021, pp. 308–310, doi: 10.1109/Metamaterials52332.2021.9577076.
[22] L. Xiang, L. Jian, and H. Xinjing, "Acoustic meta-lens for enhanced sensing consisting of single-helicoid array," *IEEE Sensors J.*, vol. 22, no. 14, pp. 13989–13998, Jul. 2022, doi: 10.1109/jsen.2022.3181981.
[23] J. W. Kim, G. Hwang, S. J. Lee, S. H. Kim, and S. Wang, "Three-dimensional acoustic metamaterial Luneburg lenses for broadband and wide-angle underwater ultrasound imaging," *Mech. Syst. Signal Process.*, vol. 179, Nov. 2022, Art. no. 109374, doi: 10.1016/j.ymssp.2022.109374.
[24] Y. Chu, T. Chen, and D. Yu, "Acoustic enhancement and weak signal detection based on the space-coiling gradient acoustic grating," *Appl. Phys. Exp.*, vol. 13, no. 9, Sep. 2020, Art. no. 097002, doi: 10.35848/1882-0786/abb0a4.
[25] J. Zhu et al., "Acoustic rainbow trapping," *Sci. Rep.*, vol. 3, no. 1, Apr. 2013, Art. no. 1728, doi: 10.1038/srep01728.
[26] Y. Chen, H. Liu, M. Reilly, H. Bae, and M. Yu, "Enhanced acoustic sensing through wave compression and pressure amplification in anisotropic metamaterials," *Nature Commun.*, vol. 5, Oct. 2014, Art. no. 5247, doi: 10.1038/ncomms6247.
[27] T. Chen and D. Yu, "A novel method for enhanced demodulation of bearing fault signals based on acoustic metamaterials," *IEEE Trans. Ind. Inform.*, vol. 18, no. 10, pp. 6857–6864, Oct. 2022, doi: 10.1109/tii.2022.3143161.
[28] T. Chen, C. Wang, and D. Yu, "Pressure amplification and directional acoustic sensing based on a gradient metamaterial coupled with space-coiling structure," *Mech. Syst. Signal Process.*, vol. 181, Dec. 2022, Art. no. 109499, doi: 10.1016/j.ymssp.2022.109499.
[29] T. Chen, W. Li, and D. Yu, "A tunable gradient acoustic metamaterial for acoustic sensing," *Extreme Mechanics Lett.*, vol. 49, Nov. 2021, Art. no. 101481, doi: 10.1016/j.eml.2021.101481.
[30] T. Chen, D. Yu, B. Wu, and B. Xia, "Weak signals detection by acoustic metamaterials-based sensor," *IEEE Sensors J.*, vol. 21, no. 15, pp. 16815–16825, Aug. 2021, doi: 10.1109/jsen.2021.3076860.
[31] T. Chen, J. Jiao, and D. Yu, "Broadband acoustic enhancement and weak signals detection within a gradient acoustic-grating metamaterial," *Measurement*, vol. 171, Feb. 2021, Art. no. 108817, doi: 10.1016/j.measurement.2020.108817.
[32] T. Chen, J. Jiao, and D. Yu, "Enhanced broadband acoustic sensing in gradient coiled metamaterials," *J. Phys. D: Appl. Phys.*, vol. 54, no. 8, Feb. 2020, Art. no. 085501, doi: 10.1088/1361-6463/abc6d7.
[33] W. Lu, Y. Bi, H. Jia, and J. Yang, "A size-reduced acoustic rainbow trapping structure," *J. Appl. Acoust.*, vol. 37, no. 2, pp. 214–219, Mar. 2018, doi: 10.11684/j.issn.1000-310X.2018.02.005.
[34] L. Zhao and S. Zhou, "Compact acoustic rainbow trapping in a bioinspired spiral array of graded locally resonant metamaterials," *Sensors*, vol. 19, no. 4, Feb. 2019, Art. no. 788, doi: 10.3390/s19040788.
[35] H. Xinjing, Y. Yutian, M. Jinyu, L. Jian, and R. Xiaobo, "An acoustic metamaterial-based sensor capable of multiband filtering and amplification," *IEEE Sensors J.*, vol. 20, no. 8, pp. 4413–4419, Apr. 2020, doi: 10.1109/jsen.2019.2962279.
[36] A. Yazdkhasti, "Passive and active graded-index acoustic metamaterials: Spatial and frequency domain multiplexing," Ph.D. dissertation, Dept. Mech. Eng., Univ. Maryland, College Park, MD, USA, 2022.
[37] C. A. Balanis, *Antenna Theory: Analysis and Design*, 4th ed. Hoboken, NJ, USA: Wiley, 2015.
[38] Y. Tasinkevych, A. Nowicki, and I. Trots, "Element directivity influence in the synthetic focusing algorithm for ultrasound imaging," in *Proc. 57th Open Seminar Acoust.*, 2010, pp. 197–200.
[39] W. Wang, S. Chen, and R. Wang, "A fast irregular microphone array design method based on acoustic beamforming," *IEEE Sensors J.*, vol. 23, no. 6, pp. 6156–6168, Mar. 2023, doi: 10.1109/JSEN.2023.3240888.
[40] B. C. Benedict, M. M. Ghanbari, and R. Muller, "Phased array beamforming methods for powering biomedical ultrasonic implants," *IEEE Trans. Ultrason., Ferroelect., Freq. Control*, vol. 69, no. 10, pp. 2756–2765, Oct. 2022, doi: 10.1109/TUFFC.2022.3197705.
[41] S. Laureti, M. Mercuri, D. A. Hutchins, F. Crupi, and M. Ricci, "Modified FMCW scheme for improved ultrasonic positioning and ranging of unmanned ground vehicles at distances < 50 mm," *Sensors*, vol. 22, no. 24, Dec. 2022, Art. no. 9899, doi: 10.3390/s22249899.

Zan Li received the B.E. and M.E. degrees in instrument science and technology in 2019 and 2022, respectively, from Tianjin University, Tianjin, China, where he is currently working toward the Ph.D. degree with the State Key Laboratory of Precision Measurement Technology and Instruments. His research interests include acoustic sensing and acoustic metamaterials.

Jinyu Ma received the B.E. and M.E. degrees in instrument science and technology from the Shandong University of Science and Technology, Qingdao, China, in 2010 and 2012, respectively, and the Ph.D. degree in instrument science and technology from Tianjin University, Tianjin, China, in 2016. In 2016, she joined Sensor and Electronic Testing Laboratory, Tianjin University as a Lecturer and an Engineer. She is also with the State Key Laboratory of Precision Measurement Technology and Instruments, Tianjin University. Her main research interests include electric sensing and measurement, precision measuring circuit, measurement, and control based on embedded system.

Jian Li received the B.E., M.E., and Ph.D. degrees in instrument science and technology from Tianjin University, Tianjin, China, in 1994, 1997, and 2000, respectively. He is currently a Full Professor with the School of Precision Instrument and Opto-Electronics Engineering, Tianjin University. He is also with the State Key Laboratory of Precision Measurement Technology and Instruments, Tianjin University. His main research interests include test signal processing, weak signal detection, and target detection technology and instruments.

Xinjing Huang received the B.Sc. and Ph.D. degrees in instrument science and technology from Tianjin University, Tianjin, China, in 2010 and 2016, respectively. In 2016, he joined the Modern Acoustic Testing Laboratory, Tianjin University as an Assistant Professor. Since 2020, he has been an Associate Professor with the School of Precision Instrument and Opto-Electronics Engineering, Tianjin University. He is also with the State Key Laboratory of Precision Measurement Technology and Instruments, Tianjin University. His main research interests include structural health inspection and/or monitoring technology, acoustic metamaterial device and sensor, magnetic/acoustic sensing and measurement, and intelligent perception electronic system.